# ARTICLE IN PRESS

Journal of Building Engineering xxx (xxxx) xxx



Contents lists available at ScienceDirect

# Journal of Building Engineering

journal homepage: www.elsevier.com/locate/jobe



# Finite element modeling of tessellated beams

Mohamed Ezz Abdelmoneim Elsayed <sup>a</sup>, Grace F. Crocker <sup>b,\*</sup>, Brandon E. Ross <sup>b</sup>, Pinar Okumus <sup>a</sup>, Michael Carlos Kleiss <sup>b</sup>, Negar Elhami-Khorasani <sup>a</sup>

#### ARTICLE INFO

# Keywords: Tessellation Finite element analysis Gap opening Tile interaction Interlocking MDF

#### ABSTRACT

Tessellated Structural-Architectural (TeSA) systems are composed of repeated tiles that can interconnect, be designed to have load carrying capacity, and are aesthetically pleasing. TeSA systems may localize damage to few tiles when subjected to extreme loads, may facilitate easier or faster reparability, and contribute to resilience. This research investigates numerical modeling of simply supported TeSA beams. Finite Element (FE) analysis was performed and the results were validated using experiments of TeSA beams made of Medium Density Fiberboard (MDF). The FE analysis incorporated gaps and interaction between tiles. The results showed that contact properties and gap size between tiles affected the calculated load-displacement relationship and strain of the TeSA beam. Contact properties were captured by a pressure-overclosure relationship, which required calibration using the global load-displacement response obtained from testing. Incorporation of geometric nonlinearity did not affect the results significantly. Beams with varying friction coefficient between tiles, load and support bearing width, Poisson's ratio and aspect ratios were analyzed. The results showed that TeSA beams had smaller stiffness than solid beams with similar dimensions. The outcomes of this research provide insights on the behavior and modeling of TeSA structures.

# 1. Introduction

This paper studies the behavior of Tessellated Structural-Architectural (TeSA) beams using numerical modeling. A tessellation is an arrangement of shapes closely fitted together in a repeated pattern without gaps or overlaps. Historically, tessellations were used mainly as aesthetic elements in buildings. Examples of architectural tessellations include the Alhambra palace in Granada, Spain [7], and the Mosque of Ibn Tulun in Cairo, Egypt [5]. Tessellations have also been recently used in building envelopes for natural light control, e.g., the Arab World Institute in Paris, France [25] and Al Bahar towers in Abu Dhabi, United Arab Emirates [2]. In this study, tessellations are used both as structural and architectural elements.

Tessellations can be non-interlocking or interlocking. Topologically interlocking tessellations transfer load through the tiles by shear, bending, and axial forces generated by the contact between tiles. On the other hand, load transfer between tiles in non-interlocking tessellations requires adhesive materials or mechanical connections. Examples of non-interlocking and interlocking tessellations are shown in Fig. 1. In this paper, 2D interlocking tessellations are considered, for which the contact between tiles does not allow for separation in either of the two orthogonal directions [12].

Small scale studies on topologically interlocking tiles showed that tessellated structures are more damage tolerant compared to the

\* Corresponding author.

E-mail address: gfulmer@clemson.edu (G.F. Crocker).

https://doi.org/10.1016/j.jobe.2021.103586

Received 22 July 2021; Received in revised form 27 September 2021; Accepted 3 November 2021

Available online 17 November 2021

<sup>&</sup>lt;sup>a</sup> University at Buffalo, United States

<sup>&</sup>lt;sup>b</sup> Clemson University, United States

same size solid structures [8,11,22]. Cracks in damaged tiles are contained in the boundaries and do not propagate to nearby tiles as seen in solid structures [12,13,18]. In addition, damaged tiles were replaced by intact ones and resulted only in limited performance loss in the small scale structure [17].

Previous research mostly focused on small scale topologically interlocked systems [4,15,20,24]. There is a need to investigate tessellations at scales suitable for building structures. Three papers have been previously published on this concept [6,19,23]. These papers discuss the concept of TeSA systems as applied to a reinforced concrete shear wall, and as part of a building structural system. They concluded that although TeSA walls have smaller stiffness and strength than conventional walls, they can be used as lateral load resisting elements with adjustments to design. The practical benefits and challenges of designing and constructing a reinforced concrete TeSA shear wall specimen were also discussed in detail. The experimental results of testing the specimen shown in Fig. 2 in reverse cyclic loading will be discussed in a forthcoming paper. Investigation of the numerical modeling of such a wall showed that wall strength can be reasonably predicted using equilibrium based approaches.

Research presented in this paper builds upon the studies by Refs. [19,23] and focuses on the numerical modeling of 2D interlocking tessellated beams for application at the building scale. The modeling approach was validated using the results of an experimental study on a Medium Density Fiberboard (MDF) beam. MDF was a convenient and efficient material choice for the test specimen because it was cost efficient and could be fabricated using a CNC machine. The experiment facilitated the primary goal of this study, which is understanding the behavior of TeSA beams through a numerical finite element (FE) study and identifying the parameters that have a strong influence on the model accuracy.

#### 2. The TeSA beam

The TeSA beam that was numerically investigated in this study was tested to failure under monotonic, quasi-static, four-point loading and failed at 36.9 kN (8.3 kips). The dimensions of the TeSA beam, loading and support conditions are shown in Fig. 3. The tessellated pattern was designed by an architecture student at Clemson University and was selected for simplicity and the ability to fabricate using an available CNC machine. The beam was tested using a universal test machine in displacement-control mode. A steel spreader beam was used to apply two symmetric load points at the top of the specimen. Load, displacement, gap opening, and strain data were collected.

The TeSA beam consisted of two types of 2D interlocking tessellations: web tiles and edge tiles. Each tile was built of 4 layers of 19 mm (0.75 in.) thick MDF sheets. The sheets were adhered together prior to CNC cutting. The dimensions of the tiles are shown in Fig. 4. The edge tiles were two times longer than the web tiles and were intended to form a flange for the beam. Two sets of edge tiles were used through thickness of the beam, while there was only one set of web tiles through the thickness. The edge tiles were staggered along the length to provide a load path across interfaces in the web tiles as shown in Fig. 3.

The material properties of MDF used to construct the specimen were determined by testing samples of the material in bending. The sample dimensions were 203 mm  $\times$  79 mm x 29 mm (8 in. x 3–1/8 in. x 1-1/8 in.) in length, width, and height, respectively.

The results of the material tests were used to develop FE model material property input. The results of the MDF TeSA beam test were used to calibrate and validate the FE model of the beam. The results of these tests will be discussed in the following sections.

# 3. Finite element model

The general FE software [1], with implicit static analysis, was used to analyze the MDF TeSA beam described above. The following sections provide details of the FE modeling.

#### 3.1. Material models

Linear-elastic material properties were assumed for MDF tiles, steel supports, and steel loading plates. The TeSA beams were made of MDF. MDF is a plane isotropic material where the properties are similar in one plane and different out of plane [14]. The loading for the beams was applied in the isotropic plane of the MDF; therefore, isotropic properties were assumed in all directions. As per [14]; the Poisson's ratio for the MDF material ranges from 0.25 to 0.32. The variation between 0.25 and 0.32 in the Poisson's ratio changes the Young's Modulus by 0.5% and was not deemed to have a significant impact on the results. The density of MDF ranges from 650 kg/m $^3$  to 800 kg/m $^3$  (41 lb/ft $^3$  to 50 lb/ft $^3$ ) [14]. A density value of 753 kg/m $^3$  (47 lb/ft $^3$ ), based on product specification of the MDF used in the tiles, was utilized to calculate the beam self-weight.

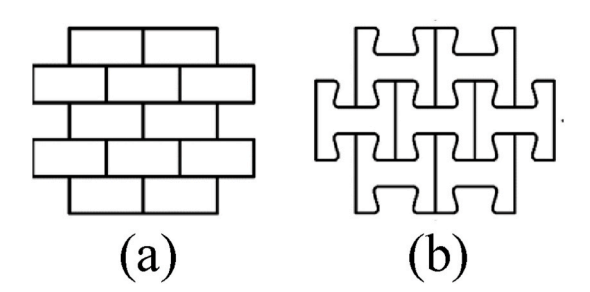


Fig. 1. (a) Non-interlocking, (b) 2D interlocking tessellations.

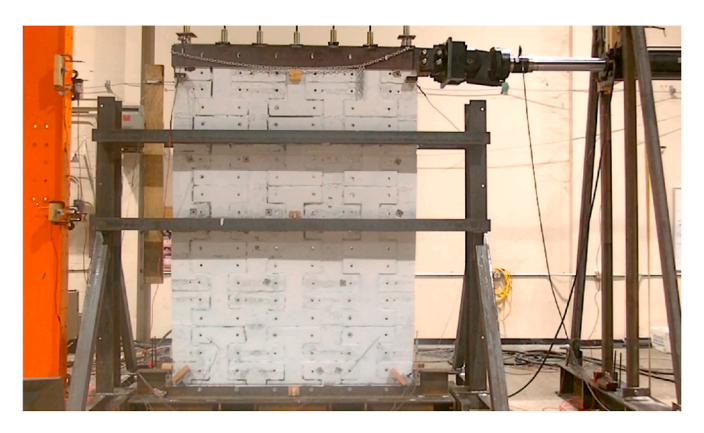


Fig. 2. Reinforced concrete TeSA shear wall specimen [6].

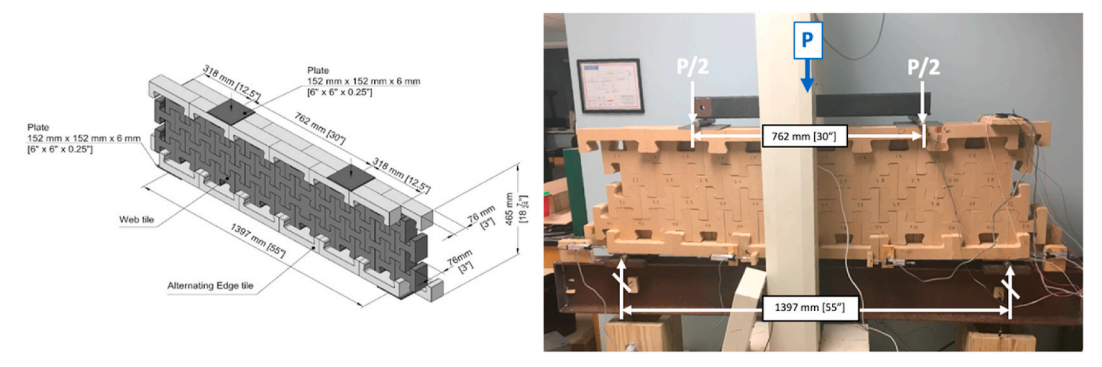


Fig. 3. Overview of the TeSA beam.

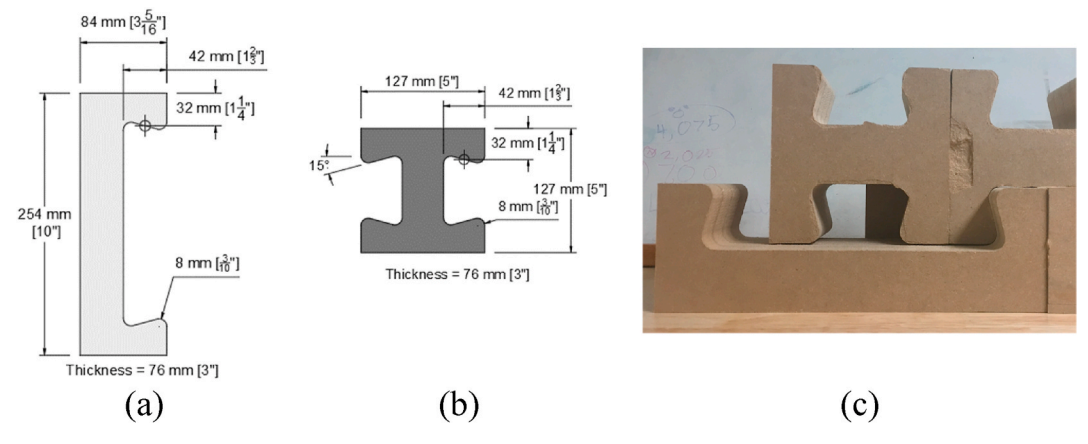


Fig. 4. (a) Edge tile dimensions, (b) web tile dimensions, (c) edge and web tiles of specimen.

The material test results discussed above were compared to a FE model. Load-displacement relationship as obtained by tile testing and tile modeling is shown in Fig. 5. The average slope of the linear part of the load displacement diagram (i.e., stiffness) from the experimental results was  $3.4 \, \text{kN/mm}$  (19.5 kip/in.). Mesh size of the FE model was  $4 \, \text{mm} \times 4 \, \text{mm} \times 4 \, \text{mm}$  (0.151 in.  $\times$  0.149 in.  $\times$  0.141 in.). The average value of Young's modulus was determined to be 2.256 GPa (327.2 ksi), taking into account the shear deformations for a simply supported beam [3] and assuming a Poisson's ratio of 0.25 [14]. The slope of the load-displacement response from the FE model was  $3.7 \, \text{kN/mm}$  (21.3 kip/in.) and was approximately 10% higher than the one obtained from testing. The higher stiffness of the FE model can be related to the idealized point load and idealized simple supports in modeling.

Loading and support plates of the beam specimen were made of steel. The material was assumed as isotropic with a Young's modulus of 200 GPa (29,000 ksi), Poisson's ratio of 0.3, and density of 7850 kg/m<sup>3</sup> (490 lb/ft<sup>3</sup>).

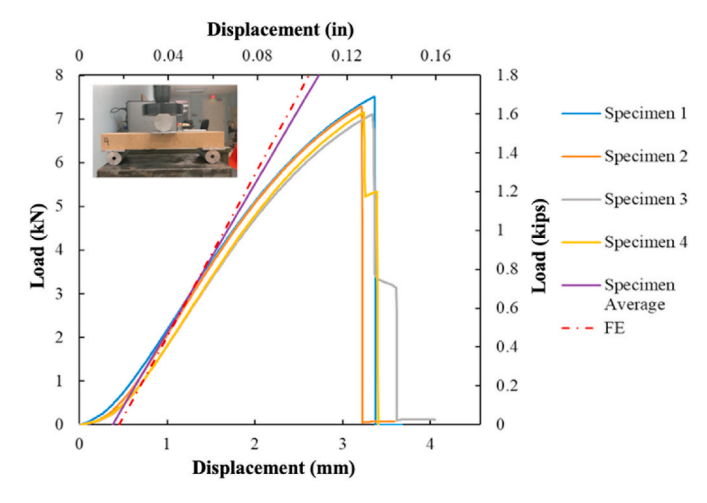


Fig. 5. Load-displacement of MDF by FE analysis and testing.

#### 3.2. Finite element type and mesh size

A combination of 8-node brick elements with reduced integration and hourglass control (called C3D8R in Abaqus) and 6-node triangular prism elements (called C3D6 in Abaqus) were used to model each tile. The majority of the elements were 8-node brick elements, while 6-node triangular prism elements were used only where the brick elements would produce a poor mesh. A 20-node quadratic brick with reduced integration (called C3D20R in Abaqus) was used to model the support and loading plates to better capture bending behavior as the plates were modeled with only one element through their thickness.

Mesh sizes for web tile, edge tile, and plates were  $11 \text{ mm} \times 10 \text{ mm} \times 9 \text{ mm} (0.417 \text{ in.} \times 0.375 \text{ in.} \times 0.361 \text{ in.}), 10 \text{ mm} \times 10 \text{ mm} \times 9 \text{ mm} (0.411 \text{ in.} \times 0.375 \text{ in.} \times 0.354 \text{ in.})$  and  $8 \text{ mm} \times 8 \text{ mm} \times 7 \text{ mm} (0.3 \text{ in.} \times 0.3 \text{ in.} \times 0.25 \text{ in.})$ , respectively. As shown in Fig. 6, care was taken to align the nodes of adjacent tiles in order to improve contact simulation. The mesh size was selected based on a mesh sensitivity analysis [10]. Comparison of the load-displacement results for a mesh size twice as fine and twice as coarse as the selected mesh size confirmed convergence in the FE results.

#### 3.3. Boundary conditions, constraints and load application

The support plates in the FE model were supported by roller supports at their centerline to replicate the simple support conditions used in testing. Since the supporting plates were allowed to displace in the direction of the beam, a constraint was introduced to force the displacement of the left support in this direction to be equal but in the opposite direction to that of the right support to ensure stability in the FE model. Out of plane displacements were restrained.

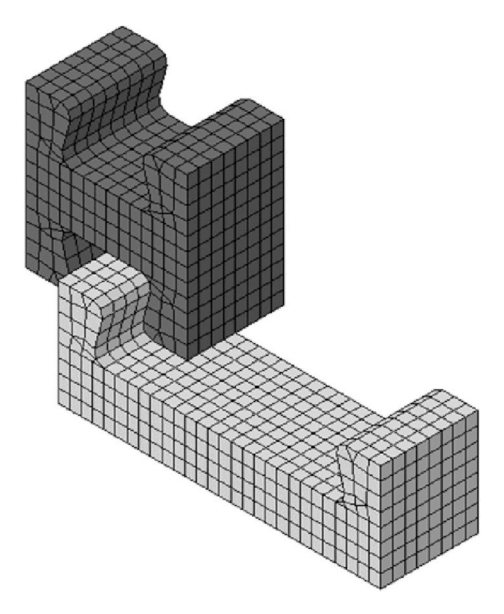


Fig. 6. FE mesh of tiles.

Sliding between the beam and load/support plates was prevented by defining tie constraints between the beam and the load/support plates.

The beam self-weight was applied as a gravity load in the first analysis step. Equal and monotonically increasing displacements were then applied at the center of each loading plate shown in Fig. 3. Boundary conditions, contact interfaces between tiles, and loads used in the model are shown in Fig. 7.

#### 3.3.1. Contact between tiles

Contact elements were used between the MDF tiles with tangential and normal behavior to simulate the interaction between the tiles. For the tangential behavior, penalty friction formulation was used with a friction coefficient of 0.25. The influence of friction coefficient on results was investigated.

Gaps between tiles, forming due to construction tolerances and deflection under self-weight, were modeled using a general contact algorithm in Abaqus that allowed two adjacent tiles to overclose when they were pushed against each other, and hence simulate the gaps closing. This contact algorithm had a "softened" pressure – overclosure relationship, which represented a stiffness relationship between the pressure applied on the contact element and the resulting overclosure between the tiles. The relationship was assumed as bilinear, as shown in Fig. 8. The initial relationship between the pressure and overclosure is represented as stiffening of the gaps when they close. Complete closing of the gaps is then represented with an infinite stiffness at a given overclosure. The point that defines the transition between the two behaviors (marked as the transition point in Fig. 8) is required as an input to the model and was investigated as a parameter in the next section.

#### 4. Modeling approaches for TeSA beams

Unlike solid beams, TeSA beams rely on load transfer between tiles, enabled by gap opening, gap closing, and friction. Small gaps are expected between tiles of TeSA beams to satisfy construction tolerances. Changes in gap sizes during loading may create nonnegligible displacements. This section investigates the effects of the following on FE analysis results: 1) including initial gaps between tiles, 2) varying friction coefficient, 3) including geometric nonlinearities (large deformations).

[9] discusses the effect of gap opening on the out-of-plane behavior of tessellated structures but only focuses on gap opening due to loading. In contrast, our study discusses the impact of pre-existing gaps due to construction tolerances and their closure due to loading, as well as tessellated beam behavior and gap opening under in-plane loading. FE modeling approaches are evaluated by comparing model results with those of the experiment.

## 4.1. Tile contact properties

Gaps between the tiles form due to construction tolerances and displacement under self-weight. The FE analysis of the TeSA beam was performed with varying contact "transition point" (Fig. 8) pressure and gap opening values, and without gaps between tiles to understand the impact of contact properties on model results. For the MDF test specimen, gaps were measured to range from 0.0508 mm to 3.0988 mm (0.002 in.–0.122 in.). Fig. 9 shows the gaps between the tiles of the specimen and a histogram of the gap sizes

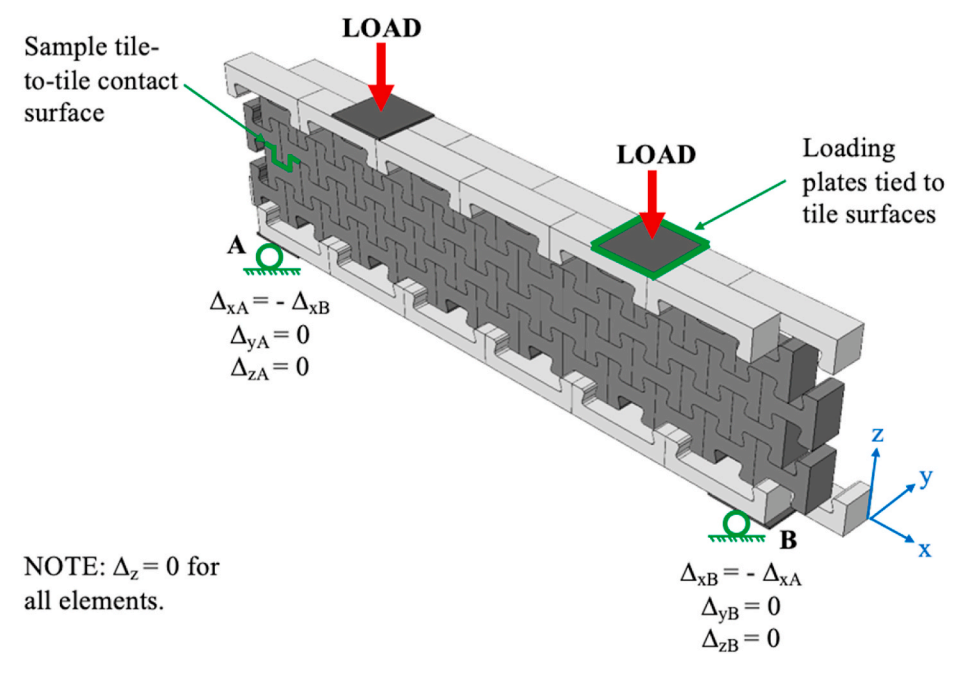


Fig. 7. Boundary conditions and loads used in the FE model.

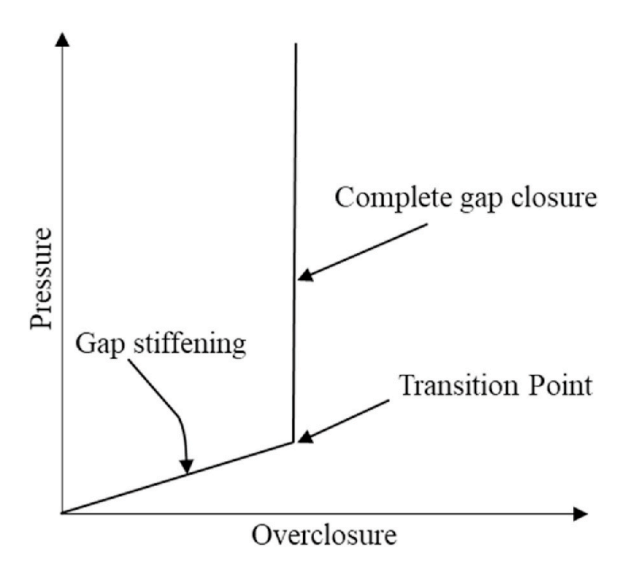


Fig. 8. Softened pressure-overclosure relationship.

measured in the test specimen. Gap sizes tended to be larger at the bottom of the specimen due to the beam's self-weight.

For analyses that considered gaps, a single gap size was used for all tiles, given that gap sizes were randomly distributed across the test beam. When investigating the transition point of contact (Fig. 8), the gap size was varied from 0.224 mm to 0.450 mm (0.0088 in.–0.0176 in.), and pressure was varied from 6.9 kPa to 34.5 kPa (1 psi to 5 psi). The selected range of gap sizes was within the range of gaps measured in the TeSA beam specimen (future applications could use a probabilistic distribution to generate random gap sizes for the model). For analyses that considered no gaps between tiles, a "hard" pressure – overclosure relationship was used in the normal direction to tile surfaces as shown in Fig. 10. The "hard" relationship prevents overlapping of the tiles.

Fig. 11 compares the load-displacement results obtained from the test and the FE model with varying gaps (i.e., varying gap size, S, and pressure, P, for contact transition point), and without gaps. The analysis with no gaps overestimated the initial stiffness significantly, although the slope of the load-displacement curve at larger displacements obtained from the FE model with no gaps was approximately parallel to the one obtained from testing. Including gaps in the analyses provided the necessary shift of the load-displacement curve towards the right to better match test results. When analyses with gaps were compared, it was shown that increasing the transition point contact pressure decreased the initial stiffness of TeSA beams. For example, when the transition contact pressure was increased from 6.9 kPa (1 psi) to 20.7 kPa (3 psi), the load-displacement curve shifted to the right by approximately 1 mm. This decrease in stiffness can be attributed to the delay in closing of gaps until a higher transition point pressure (Fig. 8) is achieved. Doubling the gap size at the transition point decreased stiffness; however, the effect of transition point gap size on the initial stiffness was not as pronounced as the effect of transition point contact pressure.

The results were also compared using a statistical measure, i.e.,  $R^2$  as defined in Equations (1)–(4), where  $FE_i$  is the predicted values from FE analysis at force increment i,  $TEST_i$  is the measured values from experiment at force increment i, and N is the number of equally spaced force increments that was taken as 201. Values of  $R^2$  closer to 1.0 indicate a better match between test and FE results.

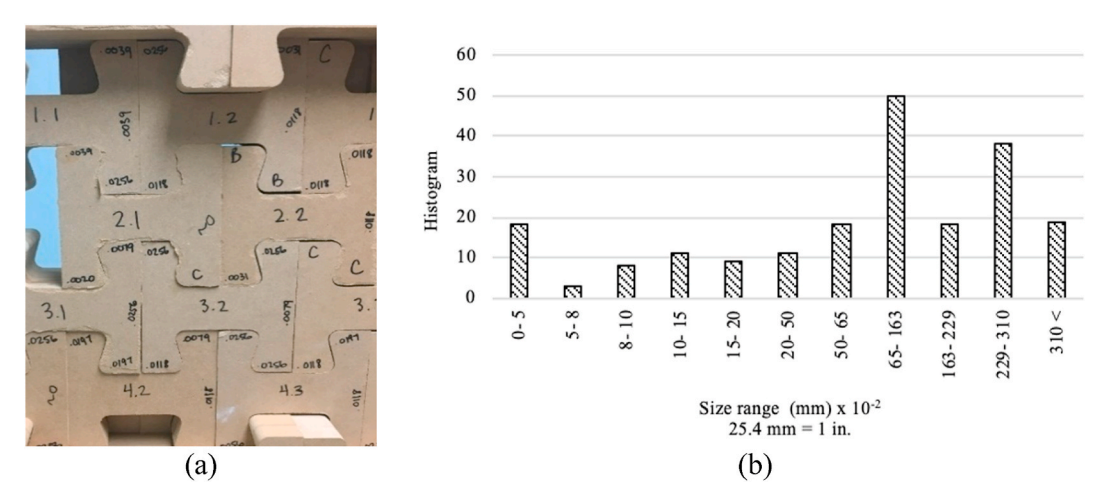


Fig. 9. (a) Gaps between tiles, (b) histogram of measured gap sizes.

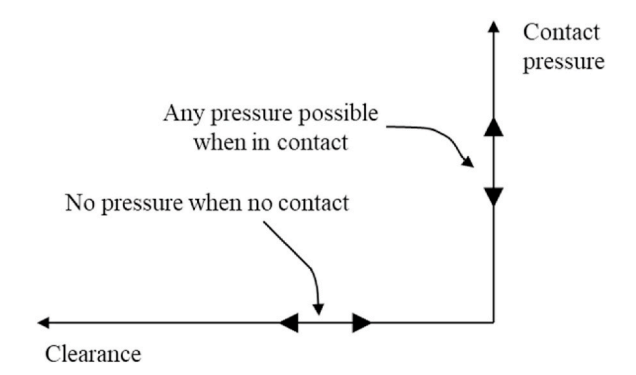


Fig. 10. Hard pressure-overclosure relationship [16].

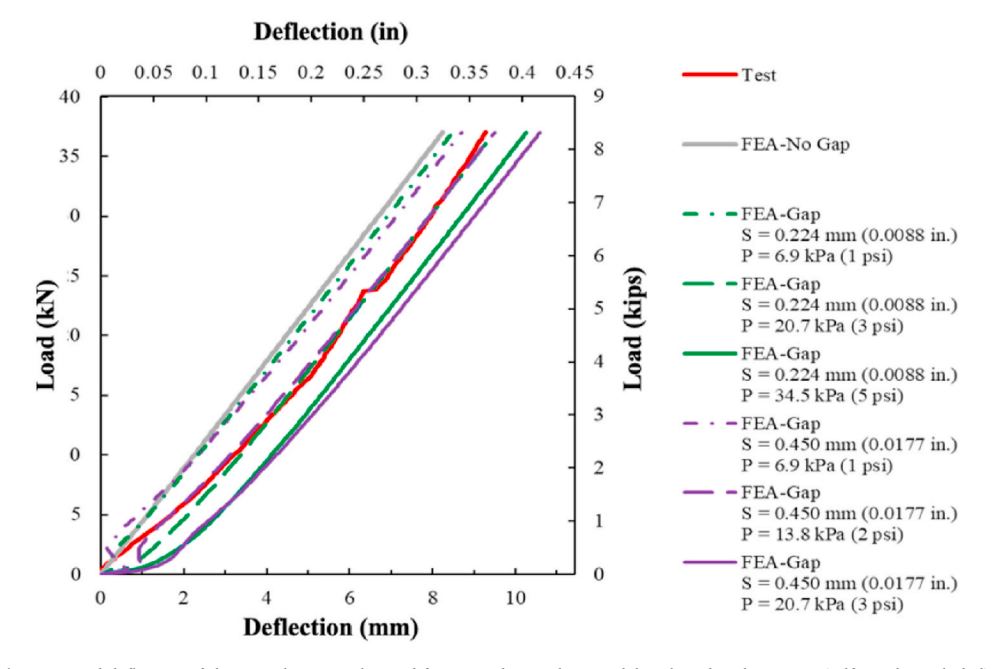


Fig. 11. Load-deflection of the TeSA beam as obtained from test data and FE model with and without gaps (self-weight excluded).

$$R^2 = 1 - \frac{SS_{res}}{SS_{tot}} \tag{1}$$

$$SS_{res} = \sum_{i} (FE_i - TEST_i)^2$$
 (2)

**Table 1**Comparison of test data and FE models with various gap properties.

Transition point property					$R^2$
Gap size		Pressure			
Mm	in. x10 <sup>-3</sup>	kPa	Psi		
No Gap					0.80
0.224	8.8	6.9	1	0.86	
0.224	8.8	20.7	3	0.99	
0.224	8.8	34.5	5	0.89	
0.450	17.7	6.9	1	0.90	
0.450	17.7	13.8	2	1.00	
0.450	17.7	20.7	3	0.84	

Journal of Building Engineering xxx (xxxx) xxx

M.E. Abdelmoneim Elsayed et al.

$$SS_{tot} = \sum_{i} \left( FE_i - \overline{FE} \right)^2 \tag{3}$$

$$\overline{FE} = \frac{1}{N} \sum_{i=1}^{N} FE_i \tag{4}$$

The results are presented in Table 1. Two gap properties, 1) a gap size of  $0.224 \, \text{mm}$  ( $0.0088 \, \text{in.}$ ) and pressure of  $20.7 \, \text{kPA}$  (3 psi) and 2) a gap size of  $0.450 \, \text{mm}$  ( $0.0176 \, \text{in.}$ ) and pressure of  $13.8 \, \text{kPA}$  (2 psi), resulted in a reasonable match with the load-midspan displacement response of the TeSA beam.

In addition to comparing FE results to load-midspan deflection, the analysis results were also compared to strains, horizontal movement at supports and gap openings measured by the TeSA beam test. The naming convention, location and function of these sensors are shown in Fig. 12 and Table 2.

Comparisons of the measured strains, gap opening and displacements to the ones obtained from the model indicated that using a gap size of 0.224 mm (0.0088 in.) and pressure of 20.7 kPA (3 psi) in the models led to the best match between FE analysis and test results. Fig. 13 compares FE analysis and test results for this transition point gap size and pressure. FE analysis results had a reasonable match with all sensor measurements, except for strain measurements at A7, C5, C9 and B3. This may be due to faulty sensors or localized strains in testing that are hard to capture by FE analysis.

In general, the low initial stiffness of the TeSA beam, which is a result of closing gaps, can be mitigated by using a filler material in the gaps with weak adhesive properties to allow the damage to be contained and prevent damage propagation from one tile to another [8,11]. This is similar to steel structures where bolted joints are required to be pretensioned whenever slip can be detrimental for the structural performance.

#### 4.2. Friction coefficient

The friction coefficient for wood ranges between 0.25 and 0.50 [21]. A study was conducted in order to determine if the friction coefficient value had an effect on the behavior of the TeSA beam. The friction coefficient was varied between 0.25 and 0.50 and the load-deflection results were compared. As shown in Fig. 14, the friction coefficient has a minimal effect, less than 5%, on the load-deflection diagram. This may be due to the fact that loads are transferred between the tiles by compression rather than shear forces. Gap opening may also be preventing friction forces to be developed between tiles as the contact area is reduced. For the rest of the analyses presented in this paper, the assumed friction coefficient was 0.25.

#### 4.3. Geometric nonlinearity

This section investigates the influence of geometric nonlinearity (large deformations) on FE results. In geometrically nonlinear analysis, load increments are applied on the deformed geometry of the structure. Although the computational cost of geometrically nonlinear analyses is higher, these analyses can provide higher accuracy when large deformations, such as the ones created by gap opening, are expected. Results of analyses with and without geometric nonlinearity were compared. The analyses had a transition point gap size of 0.22 mm (0.0088 in.), contact pressure of 20.7 kPA (3 psi), and a friction coefficient of 0.25, as described in the previous sections.

Fig. 15 compares the relationship of load and mid-span deflection from the FE model and experiment. Considering geometric nonlinearity in the analysis led to less than 5% difference in prediction of the peak load, but increased the computation time to three

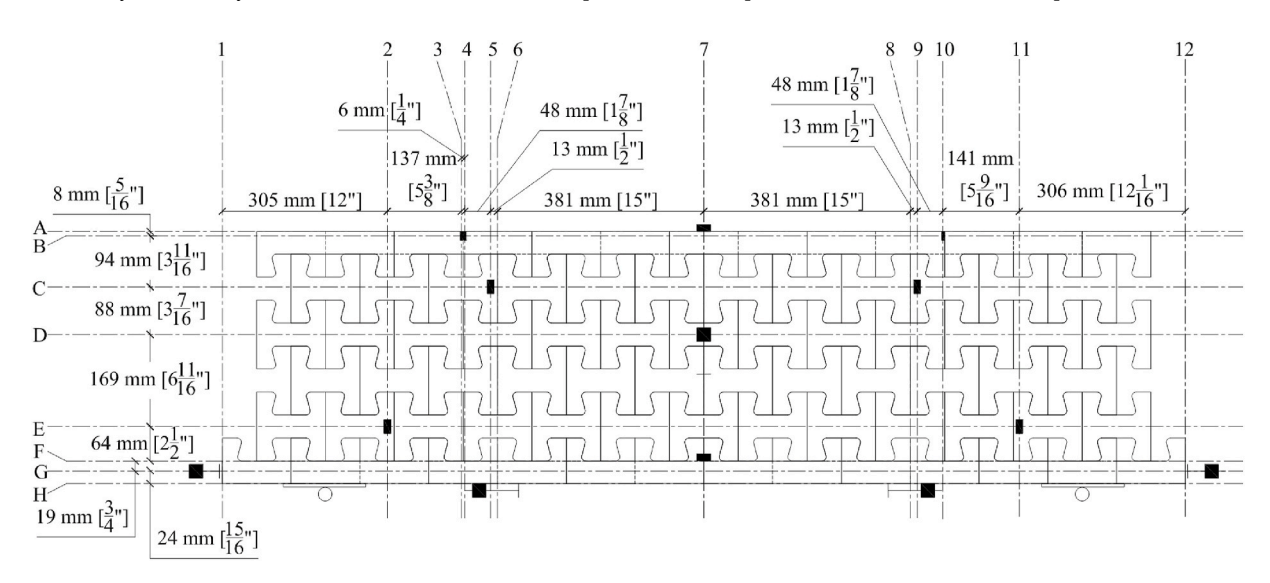


Fig. 12. Sensor locations

Table 2
Sensor locations and functions.

Sensor name (gridline)	Туре	Function
A7	Strain gage	Horizontal strain
F7	Strain gage	Horizontal strain
C5	Strain gage	Vertical strain
C9	Strain gage	Vertical strain
E2	Strain gage	Vertical strain
E11	Strain gage	Vertical strain
B4	Strain gage	Vertical strain
B10	Strain gage	Vertical strain
В3	Strain gage	Vertical strain
Н6	Linear potentiometer	Gap opening
Н8	Linear potentiometer	Gap opening
G1	Linear potentiometer	Horizontal movement
G12	Linear potentiometer	Horizontal movement
D7	Linear potentiometer	Vertical movement

times of that required without geometric nonlinearities. Therefore, geometric nonlinearity was not considered for the rest of the analyses presented in this paper.

#### 5. Analysis of TeSA beam behavior

In the previous sections, a modeling approach to characterize behavior of the TeSA beam is established. This approach includes modeling gaps between tiles, with an appropriate gap and contact pressure at the transition point when gaps completely close: 0.224 mm (0.0088 in.) and 20.7 kPA (3 psi), respectively. The friction coefficient between tiles had a minor influence on results. The effect of geometric nonlinearity was determined to be negligible and is not considered. With these model inputs, the FE analysis had a reasonable match to TeSA beam test results. In this section, principal stress magnitudes, principal stress directions and failure mechanisms are investigated.

#### 5.1. Principal stresses

Principal stresses were investigated to understand the load distribution and damage pattern in the TeSA beam. Fig. 16 shows principal tensile and compression stresses of the front face of the TeSA beam as obtained from the analyses at 36.9 kN (8.3 kips) of load, which corresponds to the failure load from testing. TeSA beam back face stresses were similar and are not shown here. Positive stresses indicate tension.

As expected, Fig. 16 shows that tiles towards the bottom of the beam, including the edge tiles, experience the highest tensile stresses. The beam experiences compression at the top, representing bending. There is also diagonal tension and diagonal compression between the locations of applied load and the supports, representing shear transfer. Because the edge tiles were staggered and two times longer than the web tiles, an alternating pattern of stress is observed in the web tiles. The edge tiles on tension side show a bowed shape because of the eccentric contact with the web tiles, which produces bending.

Fig. 16 also shows that stress is localized in each tile. For example, in the bottom row of tiles, the point of maximum stress in a web tile borders small stresses in an adjacent edge. This indicates that failure may be localized.

#### 5.2. Failure mechanism

The analyses presented in this paper were linear-elastic and not intended to capture material softening or failure. However, since the load-displacement behavior observed by testing is approximately linear up to failure, the high stress locations in the FE analysis provide indicators of expected failure locations.

The FE analysis showed that failure is expected at the bottom of the beam since the tension at the bottom of the beam translates to local shear and bending of the flanges of tiles. Local shear and bending are not developed at the top of the beam under compression, as in this region tiles bear on each other. Principal tensile stresses in the tiles near the bottom of the beam are shown in Fig. 17 at the load that caused failure of the beam during testing. Directions of principal tensile strains in a web tile are also shown, where red and blue arrows indicate tension and compression, respectively. Stresses in web tiles and adjacent edge tiles where maximum stresses were observed are approximately equal. Hence the first localized failure could be expected in either tile. The directions of principal tensile stresses indicate that the failure may be mainly due to shear stresses. This is consistent with the failure pattern observed in testing as shown in Fig. 18.

In the laboratory test, the TeSA beam failure started from a web tile on the bottom row near the mid-span, and failure propagated to the top of the beam. The failure was diagonal in all the web tiles, which may indicate a shear failure. The failure path is shown in Fig. 18. The failure was localized to 4 out of 75 tiles, which may enable reparability of the TeSA beam by replacing the damaged tiles. In addition, failure of individual tiles was often triggered by interface shear failures between plies of the MDF material as shown in Fig. 18, particularly when not all plies interlocked with the adjacent tiles as in the staggered edge tiles. This effect is not captured by the homogeneous material used in the FE.

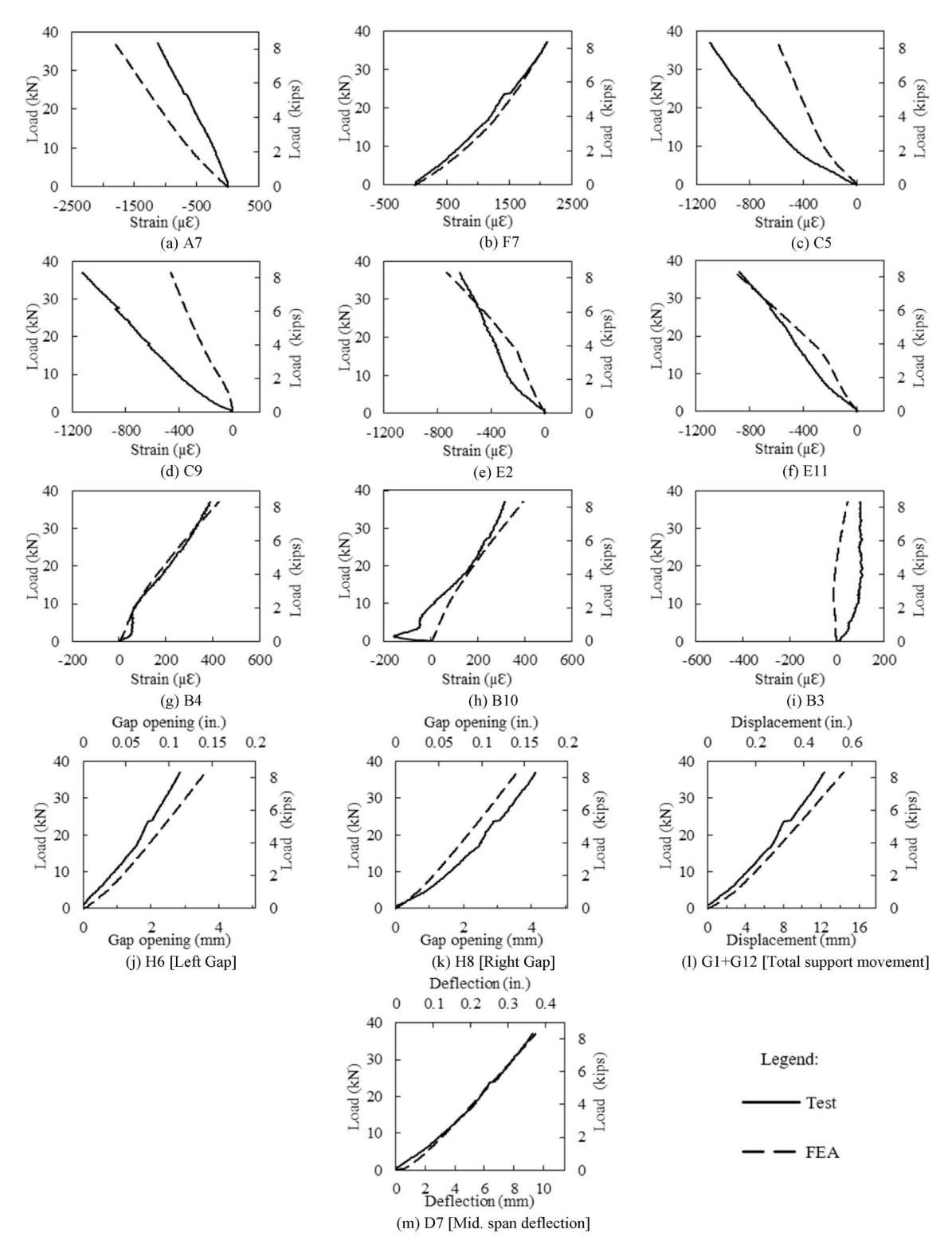


Fig. 13. Comparison of test and FE model results for local strain and displacement measurements, transition point: gap size = 0.224 mm (0.0088 in.), pressure = 20.7 kPa (3 psi).

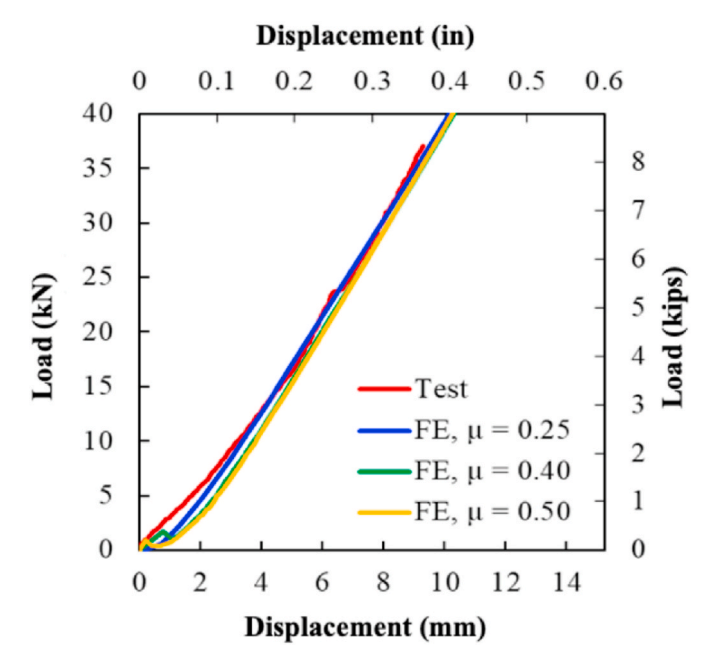


Fig. 14. Effect of friction coefficient on load-displacement response.

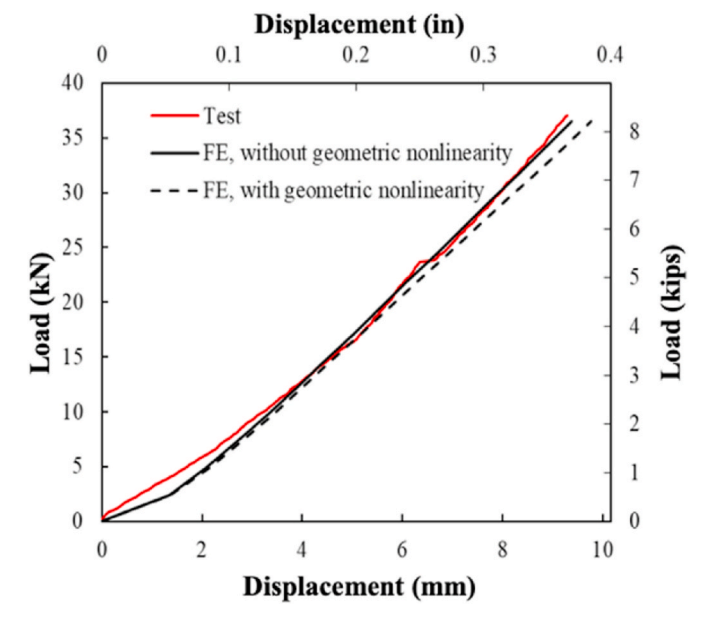


Fig. 15. Effect of geometric nonlinearity on displacement.

## 6. Effects of number of tiles on behavior

Using the calibrated and validated FE model, the impact of number of tiles along beam length (aspect ratio) on TeSA beam stiffness is investigated. Aspect ratio, defined here as the span to depth ratio, was varied. The beam depth was kept constant at 465 mm (18–7/24 in.), while the span was changed from 1397 mm (55 in.) to 2921 mm (115 in.) with increments of 508 mm (20 in.). This led to aspect ratios of 3.0 (baseline beam that was tested), 4.1, 5.2 and 6.3. The distance between the loads was kept constant at 762 mm (30 in.). Fig. 19 shows the geometry of the beams, where tile dimensions are kept constant, and the load-midspan displacement response for beams with varying aspect ratios. The stiffness of the TeSA beam decreases with the increase in the aspect ratio as expected.

It is well-known that the stiffness of a beam under bending will decrease with increasing aspect ratios. However, for TeSA beams, increasing the length of the beam also requires increasing the number of tiles along the span. Therefore, the stiffnesses of TeSA beams with equivalent solid beams are compared to understand the effect of tessellations and number of tiles in the span direction, while

Journal of Building Engineering xxx (xxxx) xxx

M.E. Abdelmoneim Elsayed et al.

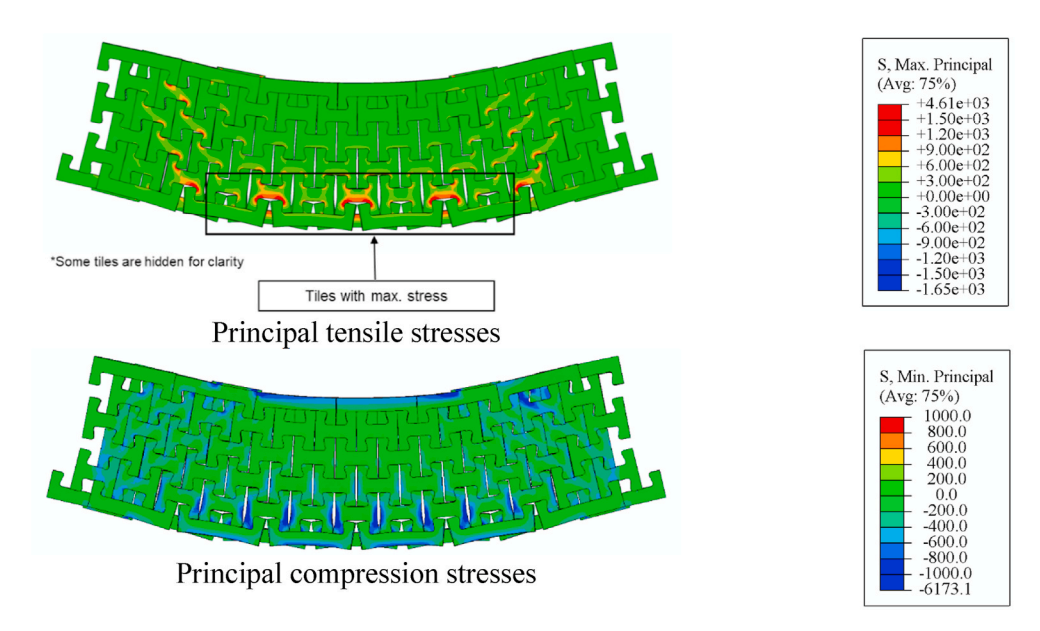


Fig. 16. Principal tensile and compressive stresses at a failure load 36.9 kN (8.3 kips).

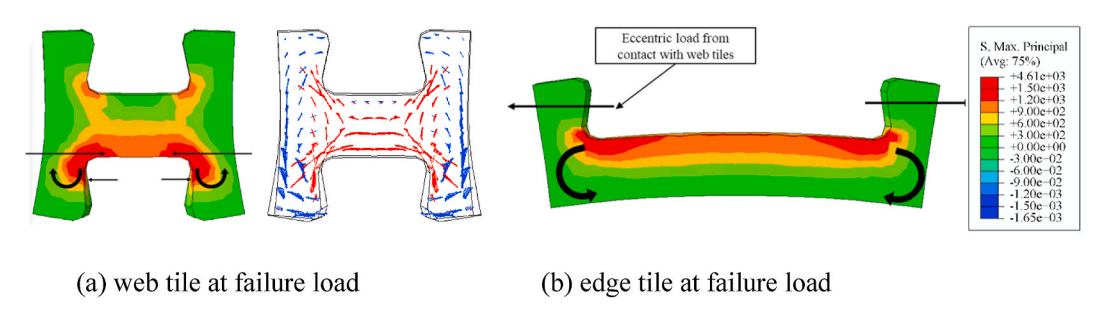


Fig. 17. Principal tensile stresses and directions on tiles at a failure load.

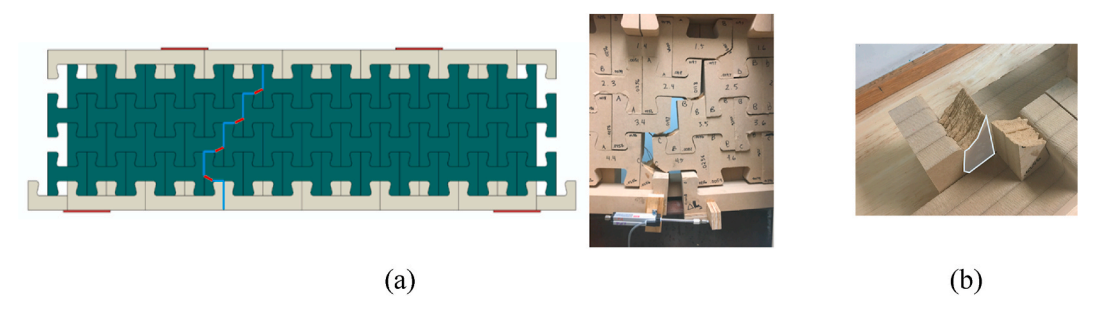


Fig. 18. (a) Failure path of tiles in test specimen, (b) interface shear failure plane.

keeping the tile size the same. Fig. 20 shows the load-deflection comparison of the TeSA beam with an aspect ratio of 3.0, with the corresponding solid beam.

It is clear that the behavior of the solid beam was linear while the TeSA beam showed nonlinear behavior initially at small forces due to existence of the gaps. The slope of the TeSA beam load-deflection diagram, beyond 4 mm (0.16 in.) of deflection (observed after the closing of the gaps), was defined as the effective stiffness of the TeSA beam. The effective stiffness of the TeSA beam was smaller than that of the solid beam.

Table 3 compares the effective stiffness of the solid and TeSA beams for varying aspect ratios. It can be concluded that the effective stiffness of the TeSA beam is approximately 10% of the solid beam for the beam configuration under study. The ratio of stiffness of TeSA beams to solid beams does not decrease considerably with increasing aspect ratios, indicating that the larger number of tiles in the span direction do not reduce the stiffness.

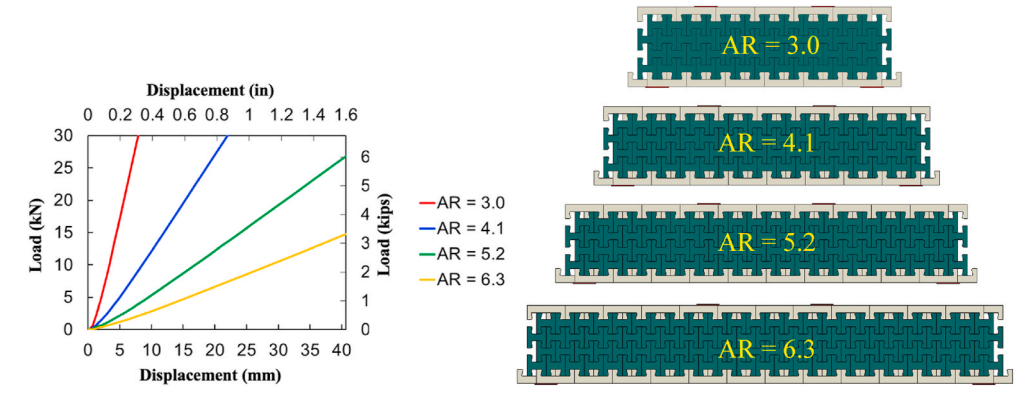


Fig. 19. Effect of aspect ratio (AR) on load-displacement.

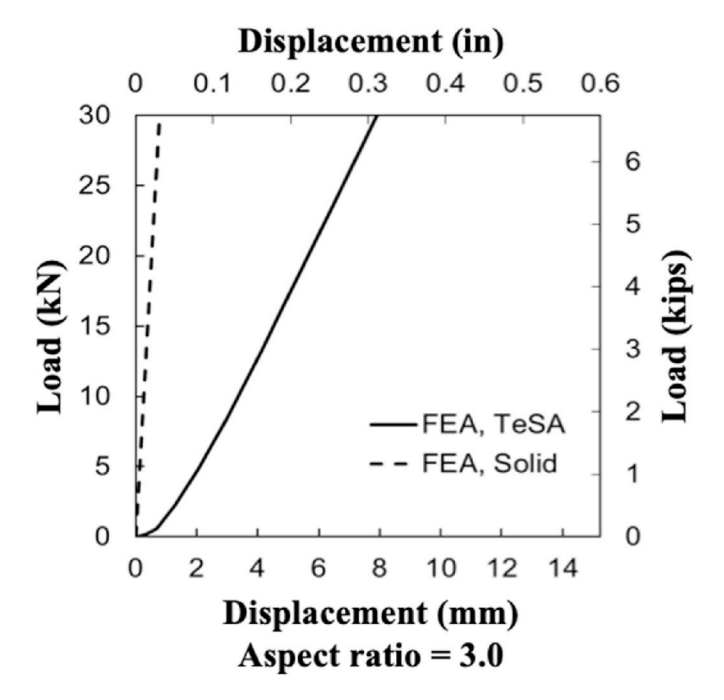


Fig. 20. Load-deflection comparison of TeSA and solid beam with aspect ratio of 3.0.

**Table 3**Stiffness comparison of TeSA and solid beams for different AR.

Span mm (in.)	No. of top row web tiles along span	Aspect ratio	TeSA beam stiffness N/mm (kip/in.)	Solid beam stiffness N/mm (kip/in.)	TeSA stiffness/Solid stiffness %
1397 (55)	12	3.0	4.4 (25.1)	38.2 (218.2)	11.5%
1905 (75)	16	4.1	1.4 (8.0)	14.5 (82.9)	9.7%
2413 (95)	20	5.2	0.7 (4.0)	7.0 (40.1)	10.0%
2921 (115)	24	6.3	0.4 (2.3)	3.9 (22.4)	10.1%

#### 7. Conclusions

This paper studied the structural behavior and modeling methods of a Tessellated Structural-Architectural (TeSA) beam using finite element analysis. The results were calibrated and validated using experimental data of a TeSA beam made of Medium Density Fiberboard (MDF). The main conclusions of this study are:

• TeSA beams are built with construction tolerances between tiles in order to facilitate assembly. Gaps between tiles affected the global behavior of the TeSA beam causing a low initial stiffness. The beam stiffness increased as gaps closed. To increase the low

Journal of Building Engineering xxx (xxxx) xxx

M.E. Abdelmoneim Elsayed et al.

initial stiffness of the beam due to gaps, a filler material for the gaps can be used. The filler material should have no or weak adhesive properties to allow the damage be contained.

- Modeling of the gaps was key to properly capture the behavior of the TeSA beam. The gaps were simulated using a calibrated
  contact element property that allows overlap of tiles when pressure is applied. One gap property across all tiles, rather the individual gap property assignments for each tile, can be used to simulate the load-displacement response of the beam with reasonable
  accuracy.
- The results were not sensitive to variations in friction coefficient of tile interfaces. This may indicate that the behavior is governed by gap opening rather than sliding between tiles.
- Including geometric nonlinearity in models made less than 5% difference in the predicted mid-span displacements but increased the computational time by a factor of 3.
- Principal stresses were localized in tiles, as observed by discontinuity of stresses between adjacent tiles.
- The tension in the bottom of the beam was translated into bending and shear in the tiles. FE analyses showed inclined directions for principal tensile stresses, which correlated with the observed diagonal failure in the tiles during the experiment.
- TeSA beams had an effective stiffness (after closing of gaps) that was approximately 10% of that for solid beams with similar dimensions. The ratio of TeSA beam stiffness to equivalent solid beam stiffness did not change considerably with the number of tiles in the span direction, which may indicate that additional tiles (and gaps) do not cause a loss of stiffness.

#### Author statement

Mohamed Ezz Abdelmoneim Elsayed: Methodology, Formal analysis, Investigation, Writing (original draft), Visualization. Grace F. Crocker: Validation, Investigation, Writing (review and editing), Visualization. Brandon E. Ross: Conceptualization, Methodology, Resources, Supervision, Project Administration, Funding acquisition. Pinar Okumus: Conceptualization, Methodology, Resources, Writing (review and editing), Supervision, Project Administration, Funding acquisition. Michael Carlos Kleiss: Conceptualization, Project Administration, Funding acquisition. Negar Elhami-Khorasani: Conceptualization, Methodology, Resources, Writing (review and editing), Supervision, Project Administration, Funding acquisition.

#### Declaration of competing interest

The authors declare that they have no known competing financial interests or personal relationships that could have appeared to influence the work reported in this paper.

#### Acknowledgements

This material is based upon work supported by the National Science Foundation under Grant Nos. 1762133 and 1762899. Any opinions, findings, and conclusions or recommendations expressed in this material are those of the authors and do not necessarily reflect the views of the National Science Foundation.

### References

- [1] Abaqus, Abaqus Finite Element Software, Version 2019', Simulia Corp., Providence, RI, USA, 2019.
- [2] Mohammad Alshami, Mohammad Atwa, Fathy Ahmad, Saleh Ahmad, Parametric patterns inspired by nature for responsive building façade, Int. J. Innov. Res. Sci. Eng. Technol. 4 (2015) 8009–8018.
- [3] ASTM, ASTM D198-15, Standard Test Methods of Static Tests of Lumber in Structural Sizes, ASTM International West Conshohocken, 2015.
- [4] Charles Brugger, Marc C. Fivel, Yves Brechet, 'Numerical Simulations of Topologically Interlocked Materials Coupling DEM Methods and FEM Calculations: Comparison with Indentation Experiments, MRS Online Proceedings Library Archive, 2009, p. 1188.
- [5] Roger Burrows, Reconstructing early islamic geometries applied to surface designs, in: Bridges 2019 Conference Proceedings, Tessellations Publishing, 2019, pp. 163–170.
- [6] Grace F. Crocker, Brandon E. Ross, Michael Carlos Kleiss, Pinar Okumus, Negar Elhami-Khorasani, John Michael Romano, Design, Fabrication, and Assembly of a Tessellated Precast Concrete Wall, Paper presented at 2021 PCI Convention, New Orleans, LA, May 2021, Precast Concrete Institute, 2021.
- [7] Douglas Dunham, Hyperbolic islamic patterns-a beginning', Bridges. ', 2001, pp. 247–254.
- [8] Arcady V. Dyskin, Yuri Estrin, J. Alexei, Kanel-Belov, Elena Pasternak, 'A new concept in design of materials and structures: assemblies of interlocked tetrahedron-shaped elements, Scripta Mater. 44 (2001) 2689–2694.
- [9] Aracady V. Dyskin, Yuri Estrin, Elena Pasternak, Chapter 2 topological interlocking materials, in: Y. Estrin, Y. Brechet, J. Dunlop (Eds.), Architectured Materials in Nature and Engineering Archimats, Springer Series in Materials Science 282, 2019, pp. 23–49.
- [10] M.E.A. Elsayed, An Analytical Study on the Structural Behavior of a Medium Density Fiberboard Tessellated Beam, University at Buffalo, the State University of, New York, 2020.
- [11] Yuri Estrin, Arcady V. Dyskin, Alexei J. Kanel-Belov, Elena Pasternak, Materials with novel architectonics: assemblies of interlocked elements, in: IUTAM Symposium on Analytical and Computational Fracture Mechanics of Non-homogeneous Materials, Springer, 2002, pp. 51–55.
- [12] Yuri Estrin, V. Arcade, Dyskin, Elena Pasternak, Stephan Schaare, Sergei Stanchits, J. Alexei, Kanel-Belov, Negative stiffness of a layer with topologically interlocked elements, Scripta Mater. 50 (2004) 291–294.
- [13] Yuri Estrin, V. Arcady, Dyskin, Elena Pasternak, Topological interlocking as a material design concept, Mater. Sci. Eng. C 31 (2011) 1189–1194.
- [14] Stefan Ganev, Gendron Guy, Alain Cloutier, Robert Beauregard, Mechanical properties of MDF as a function of density and moisture content, Wood Fiber Sci. 37 (2007) 314–326.
- [15] A Rezaee Javan, H. Seifi, S. Xu, D. Ruan, Y.M. Xie, The impact behaviour of plate-like assemblies made of new interlocking bricks: an experimental study, Mater. Des. 134 (2017) 361–373.
- [16] Abaqus Manual, Abaqus Analysis User's Manual, Version 2019', Simulia Corp., Providence, RI, USA, 2019.
- [17] Adam Mather, Cipra Raymond, Thomas Siegmund, 'Structural integrity during remanufacture of a topologically interlocked material, Int. J. Struct. Integr. (2012).
- [18] Andrey Molotnikov, Yuri Estrin, Arcady V. Dyskin, Elena Pasternak, J. Alexei, Kanel-Belov, 'Percolation mechanism of failure of a planar assembly of interlocked osteomorphic elements, Eng. Fract. Mech. 74 (2007) 1222–1232.

# ARTICLE IN PRESS

#### M.E. Abdelmoneim Elsayed et al.

Journal of Building Engineering xxx (xxxx) xxx

- [19] Brandon E. Ross, Cancan Yang, Michael Carlos Kleiss, Pinar Okumus, Negar Elhami Khorasani, Tessellated structural-architectural systems: a concept for efficient construction, repair, and disassembly, J. Architect. Eng. 26 (2020).
- [20] Stephan Schaare, Arcade V. Dyskin, Yuri Estrin, Stephan Arndt, Elena Pasternak, J. Alexei, Kanel-Belov, 'Point loading of assemblies of interlocked cube-shaped elements, Int. J. Eng. Sci. 46 (2008) 1228–1238.
- [21] R.A. Serway, J.W. Jewett Jr., Physics for Scientists and Engineers with Modern Physics, ninth ed., Cengage Learning, Boston, MA, 2013.
- [22] Thomas Siegmund, Francois Barthelat, Cipra Raymond, Manufacture and mechanics of topologically interlocked material assemblies, in: Habtour, Jaret Riddick (Eds.), Appl. Mech. Rev. 68 (2016).
- [23] Mohammad Syed, Mohammad Moeini, Pinar Okumus, Negar Elhami-Khorasani, Brandon E. Ross, Michael Carlos Barrios Kleiss, Analytical study of tessellated structural-architectural reinforced concrete shear walls, Eng. Struct. 244 (2021) 112768.
- [24] Babak Zareiyan, Behrokh Khoshnevis, 'Effects of interlocking on interlayer adhesion and strength of structures in 3D printing of concrete, Autom. ConStruct. 83 (2017) 212–221.
- [25] Machi Zawidzki, Dynamic shading of a building envelope based on rotating polarized film system controlled by one-dimensional cellular automata in regular tessellations (triangular, square and hexagonal), Adv. Eng. Inf. 29 (2015) 87–100.